INTERNATIONAL JOURNAL FOR NUMERICAL METHODS IN FLUIDS
Int. J. Numer. Meth. Fluids 2007; **53**:353–369
Published online 19 June 2006 in Wiley InterScience (www.interscience.wiley.com). DOI: 10.1002/fld.1224

Numerical predictions of flow and thermal fields in an enclosure with two periodically moving walls

Chin-Hsiang Cheng*,† and Kuo-Shu Hung‡

Department of Mechanical Engineering, Tatung University, 40 Chungshan North Road, Sec. 3, Taipei, Taiwan 10451, ROC

SUMMARY

Numerical predictions of transient flow and thermal fields in a rectangular enclosure with two periodically moving vertical walls are presented. The combined influence of the movement of the walls and the buoyancy as well on the flow pattern and heat transfer performance is evaluated. The compressible-flow model is adopted, and governing equations are expressed in integral form and discretized on the moving grids, which deform in resonance with the walls to accommodate the variation in the volume of the enclosure. A two-stage pressure-correction scheme is applied for simultaneously determining the distributions of absolute pressure, density, temperature, and velocity of the compressible flow field in the enclosure during the periodically stable periods. Effects of the frequency, stroke, and the phase angle of the wall oscillations on the flow are of major concerns in this study. The frequency is ranged between 5 and 25 Hz and the dimensionless strokes (l/H) of the wall are varied from 0.4 to 1.0. Results for Nusselt numbers on the walls as well as the dimensionless input work required to excite the wall oscillation are provided. Copyright © 2006 John Wiley & Sons, Ltd.

KEY WORDS: numerical predictions; enclosure; oscillation; heat transfer; flow pattern

INTRODUCTION

Periodic flow motion in a piston–cylinder assembly has received increasing attention in recent years due to its relevance to a number of practical devices, including internal-combustion heat engines, reciprocating compressors, and hydraulic pumps. These practical devices are equipped with moving parts, which are referred to as the moving boundaries to the internal fluid flow, and in these devices the flow problems are, in essence, more involved than those with only stationary boundaries.

*Correspondence to: Chin-Hsiang Cheng, Department of Mechanical Engineering, Tatung University, 40 Chungshan North Road, Sec. 3, Taipei, Taiwan 10451, ROC.
†E-mail: cheng@ttu.edu.tw
‡E-mail: d8801002@ms2.ttu.edu.tw

Received 2 November 2005
Revised 24 January 2006
Accepted 16 February 2006

Existing studies related to the moving-boundary problems may be categorized into two kinds in accordance with the basic approaches used to deal with the boundary movement. In the first kind of studies, the moving boundary sweeps over fixed grids in the inertial reference frame. This approach is not suitable for flows having large change in the volume of the system since the number of grids will be increased and decreased during the expansion and compression processes, respectively, and occasionally the grid number may become too large or too small to provide accurate solutions. The second kind, on the other hand, uses moving grids, which deform in resonance with the moving parts to accommodate the variation in the volume of the system. A dynamic grid-generation method is required to yield the moving grids. This approach allows a larger deformation of the volume; therefore, it is most widely used for numerical computation. Hirt *et al.* [1] proposed the arbitrary Lagrangian–Eulerian (ALE) scheme using grids of which the vertices may move with the boundary, be held fixed, or move in any other prescribed way. This report provides a fair assessment in relative performance of these two kinds of approaches.

Lately, a number of techniques using the moving grids have been developed for various applications. Demirdzic and Peric [2] extended the capability of numerical predictions of the moving-boundary flows to the problems with a domain of irregular shape. Gosman [3] developed a RPM method for predicting in-cylinder processes within a reciprocating internal-combustion engine based on the k–ε turbulence model and related wall functions. Attention of Hirt and Nichols [4] was focused on the development of a computational method by using a combination of the deforming grid and the volume-of-fluid (VOF) technique. Recently, Haworth and Jansen [5] used unstructured deforming meshes in a large-eddy simulation of reciprocating internal-combustion engine flows. Nkonga [6] used finite volume method with mesh relaxation, based on the modified linear elasticity equations, to investigate the three-dimensional flow behaviour in the combustion chamber of a four-valve piston engine.

A constraint on the moving-grid approach, which is named the geometrical/space conservation law (GCL/SCL), was first discussed by Trulio and Trigger [7]. Demirdzic and Peric [8] demonstrated that a violation of the space conservation law may result in false mass sources and lead to great errors in the analysis of moving-boundary problems. A concept of integrated space-time coordinate frame, on which the moving grids are constructed, was discussed by Zwart *et al.* [9] and Guillard and Farhat [10]. In addition, the boundary tracking methods used to satisfy the conservation laws for the compressible flows with moving boundary were presented by Falcovitz *et al.* [11], Koobus and Farhat [12], and Visbal and Gaitonde [13].

These existing numerical studies offer valuable tools for understanding the structure of moving-boundary flows and provide insight not easily obtainable with experiments. However, so far almost all the existing studies were performed for isothermal flows and focused on the velocity field only. Unfortunately, most systems encountered in practice involve a transient change in temperature field during the reciprocating compression and expansion processes. All the thermodynamic properties involving temperature of the fluid change continuously with time; therefore, the flow field inside a system cannot be determined independently without knowledge of the distributions of other thermodynamic properties of the fluid. Hung and Cheng [14] proposed a two-stage pressure-correction method which was successfully applied to carry out the simultaneous solutions for temperature, density, absolute pressure and velocity distributions in a piston–cylinder assembly. This method was also applied to evaluate the pressure effects on natural convection for the non-Boussinesq fluid in a rectangular enclosure [15].

Stirling engines are power machines that operate over a closed, regenerative thermodynamic cycle, with cyclic compression and expansion of the working fluid at different temperature levels, as described by Cheng and cowokers [16–18]. In a typical α-configuration Stirling engine, two separate pistons are equipped in a single or two separate cylinders with thermodynamic cycle taking place in the closed space between the tops of the two pistons. Stirling engine technology has come a long way in the past several decades. However, new concepts and designs continue to emerge. Recently, interest in Stirling engines has resurfaced, with solar electric power generation [19] and hybrid automotive applications in the forefront. Unfortunately, detailed information regarding the flow and thermal behaviour of the periodic flow in the two-piston engines is still not available. Under these circumstances, in the present study, the numerical method proposed by Hung and Cheng [14] is extended to the analysis of the flows in an enclosure with two periodically moving walls to seek a fundamental understanding of the physical phenomena in the two-piston engines.

This study is therefore concerned with transient variations in flow and thermal fields in a rectangular enclosure with two periodically moving vertical walls shown in Figure 1. The solution domain between the two vertical walls is of length D and height H. The left wall (wall 1) is maintained at higher temperature T_{H}, and the right wall (wall 2) is at lower temperature T_{R}. The two vertical walls move back-and-forth in between their bottom-dead (BDP) and top-dead points (TDP) independently by

$$x_1 = x_{i1} + \frac{l}{2}\sin(2\pi f t) \quad \text{for wall 1} \tag{1a}$$

$$x_2 = x_{i2} + \frac{l}{2}\sin(2\pi f t + \alpha) \quad \text{for wall 2} \tag{1b}$$

where l is the stroke and α is the phase angle of the oscillations of the walls. Note that the strokes of the two walls are equal here. However, due to the existence of phase angle, the length D is actually a function of time even though the strokes are equal. The enclosure volume experiences compression and expansion periodically due to the relative motion of the

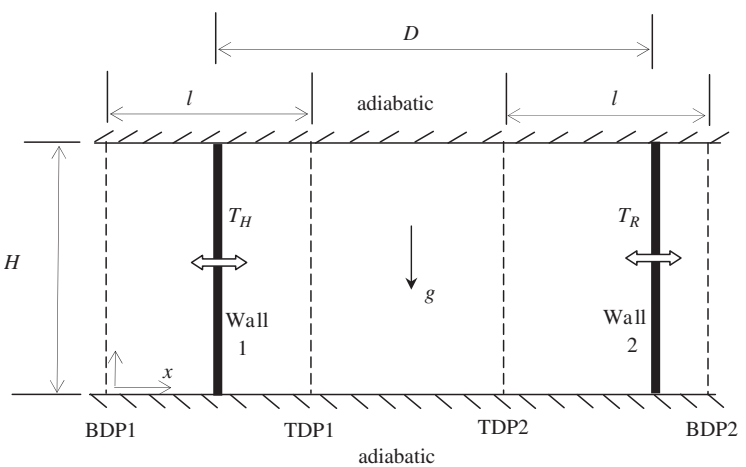

Figure 1. An enclosure with two periodically moving walls.

walls with phase angle α. On the other hand, the top and the bottom horizontal walls are stationary and adiabatic.

THEORETICAL ANALYSIS

Governing equations

It is assumed that the air in the enclosure is compressible, homogeneous, and isotropic; the flow is considered as a laminar flow and the works done by the gravitational and the viscous forces are neglected. The conservation laws of space, mass, momentum, and energy in dimensionless forms are derived as follows:

Space conservation:

$$\frac{\mathrm{d}}{\mathrm{d}\widetilde{t}}\int_{cv}\mathrm{d}\widetilde{\mathcal{V}}=\int_{cs}\widetilde{\mathbf{V}}_{\mathrm{b}}\cdot\mathrm{d}\widetilde{\mathbf{A}} \tag{2}$$

Mass conservation:

$$\frac{\mathrm{d}}{\mathrm{d}\widetilde{t}}\int_{cv}\widetilde{\rho}\,\mathrm{d}\widetilde{\mathcal{V}}=\int_{cs}\widetilde{\rho}(\widetilde{\mathbf{V}}-\widetilde{\mathbf{V}}_{\mathrm{b}})\cdot\mathrm{d}\widetilde{\mathbf{A}} \tag{3}$$

Momentum conservation for x-direction:

$$\frac{\mathrm{d}}{\mathrm{d}\widetilde{t}}\int_{cv}\widetilde{\rho}\widetilde{u}\,\mathrm{d}\widetilde{\mathcal{V}}=-\int_{cs}\widetilde{\rho}(\widetilde{\mathbf{V}}-\widetilde{\mathbf{V}}_{\mathrm{b}})\widetilde{u}\cdot\mathrm{d}\widetilde{\mathbf{A}}-\int_{cv}(\nabla\widetilde{P}\cdot\mathbf{i})\,\mathrm{d}\widetilde{\mathcal{V}}+\int_{cs}\widetilde{\mathbf{t}}_{x}\cdot\mathrm{d}\widetilde{\mathbf{A}} \tag{4}$$

Momentum conservation for y-direction:

$$\frac{\mathrm{d}}{\mathrm{d}\widetilde{t}}\int_{cv}\widetilde{\rho}\widetilde{v}\,\mathrm{d}\widetilde{\mathcal{V}}=-\int_{cs}\widetilde{\rho}\widetilde{v}(\widetilde{\mathbf{V}}-\widetilde{\mathbf{V}}_{\mathrm{b}})\cdot\mathrm{d}\widetilde{\mathbf{A}}-\int_{cv}(\nabla\widetilde{P}\cdot\mathbf{j})\,\mathrm{d}\widetilde{\mathcal{V}}+\int_{cs}\widetilde{\mathbf{t}}_{y}\cdot\mathrm{d}\widetilde{\mathbf{A}}-B\int_{cv}(\widetilde{\rho}-\widetilde{\rho}_{\mathrm{E}})\,\mathrm{d}\widetilde{\mathcal{V}} \tag{5}$$

Energy conservation:

$$\begin{aligned}\frac{\mathrm{d}}{\mathrm{d}\widetilde{t}}\int_{cv}\widetilde{\rho}\widetilde{T}\,\mathrm{d}\widetilde{\mathcal{V}}&=C_1\frac{\mathrm{d}}{\mathrm{d}\widetilde{t}}\int_{cv}\widetilde{P}\,\mathrm{d}\widetilde{\mathcal{V}}-\int_{cs}\widetilde{\rho}\widetilde{T}(\widetilde{\mathbf{V}}-\widetilde{\mathbf{V}}_{\mathrm{b}})\cdot\mathrm{d}\widetilde{\mathbf{A}}-\int_{cs}\widetilde{\mathbf{q}}\cdot\mathrm{d}\widetilde{\mathbf{A}}\\&\quad-C_1\int_{cs}\widetilde{P}\widetilde{\mathbf{V}}_{\mathrm{b}}\cdot\mathrm{d}\widetilde{\mathbf{A}}+C_2\frac{\mathrm{d}}{\mathrm{d}\widetilde{t}}\int_{cv}\widetilde{P}_{\mathrm{E}}\mathrm{d}\widetilde{\mathcal{V}}-C_2\int_{cs}\widetilde{P}_{\mathrm{E}}\widetilde{\mathbf{V}}_{\mathrm{b}}\cdot\mathrm{d}\widetilde{A}\end{aligned} \tag{6}$$

where

$$B=\frac{gH}{U_{\mathrm{R}}^2},\quad C_1=\frac{U_{\mathrm{R}}^2}{C_P T_{\mathrm{R}}},\quad C_2=\frac{R}{C_P},\quad \widetilde{\mathbf{t}}_x=[\widetilde{\tau}_{ij}]\cdot\mathbf{i},\quad \widetilde{\mathbf{t}}_y=[\widetilde{\tau}_{ij}]\cdot\mathbf{j}$$

and the components of the stress tensor $[\widetilde{\tau}_{ij}]$ are given by

$$\widetilde{\tau}_{xy}=\widetilde{\tau}_{yx}=\frac{1}{Re}\left(\frac{\partial\widetilde{v}}{\partial\widetilde{x}}+\frac{\partial\widetilde{u}}{\partial\widetilde{y}}\right),\quad \widetilde{\tau}_{xx}=\frac{2}{Re}\left(\frac{\partial\widetilde{u}}{\partial\widetilde{x}}\right)-\frac{2}{3}\frac{1}{Re}\nabla\cdot\widetilde{\mathbf{V}}$$

and

$$\widetilde{\tau}_{yy} = \frac{2}{Re}\left(\frac{\partial \widetilde{v}}{\partial \widetilde{y}}\right) - \frac{2}{3}\frac{1}{Re}\nabla \cdot \widetilde{\mathbf{V}}$$

With the help of the dimensionless ideal-gas equation

$$\widetilde{\rho} = \frac{C\widetilde{P} + \widetilde{P}_{\mathrm{E}}}{\widetilde{T}} \tag{7}$$

where $C = C_1/C_2$, the initial hydrostatic pressure expression can be given as

$$\widetilde{P}_{\mathrm{E}} = \widetilde{\rho}_{\mathrm{E}} = \mathrm{e}^{-(gH/RT_{\mathrm{R}})\widetilde{y}} = \mathrm{e}^{-F\widetilde{y}} \tag{8}$$

where $F = gH/RT_{\mathrm{R}}$. Using Equation (8), the values of $\widetilde{P}_{\mathrm{E}}$ and $\widetilde{\rho}_{\mathrm{E}}$ appearing in Equations (5) and (6) can be calculated. The above dimensionless parameters are defined by

$$\begin{aligned} &\widetilde{x} = \frac{x}{H}, \quad \widetilde{y} = \frac{y}{H}, \quad \widetilde{t} = \frac{tU_{\mathrm{R}}}{H}, \quad \widetilde{\rho} = \frac{\rho}{\rho_{\mathrm{R}}}, \quad \widetilde{\rho}_{\mathrm{E}} = \frac{\rho_{\mathrm{E}}}{\rho_{\mathrm{R}}}, \quad \widetilde{u} = \frac{u}{U_{\mathrm{R}}}, \\ &\widetilde{v} = \frac{v}{U_{\mathrm{R}}}, \quad \widetilde{T} = \frac{T}{T_{\mathrm{R}}}, \quad \widetilde{P} = \frac{P - P_{\mathrm{E}}}{\rho_{\mathrm{R}} U_{\mathrm{R}}^2}, \quad \widetilde{P}_{\mathrm{E}} = \frac{P_{\mathrm{E}}}{\rho_{\mathrm{R}} R T_{\mathrm{R}}} \end{aligned} \tag{9}$$

where $U_{\mathrm{R}} = \pi f l$, which is the characteristic velocity.

The dimensionless boundary and initial conditions for the problem can be expressed as

$$\widetilde{u} = \frac{\mathrm{d}\widetilde{x}_1}{\mathrm{d}\widetilde{t}}, \quad \widetilde{v} = 0, \quad \widetilde{T} = \widetilde{T}_1 = T_{\mathrm{H}}/T_{\mathrm{R}} \quad \text{on wall 1} \tag{10a}$$

$$\widetilde{u} = \frac{\mathrm{d}\widetilde{x}_2}{\mathrm{d}\widetilde{t}}, \quad \widetilde{v} = 0, \quad \widetilde{T} = \widetilde{T}_2 = 1.0 \quad \text{on wall 2} \tag{10b}$$

$$\widetilde{u} = \widetilde{v} = 0, \quad \frac{\partial \widetilde{T}}{\partial \widetilde{y}} = 0 \quad \text{on top and bottom walls} \tag{10c}$$

with

$$\widetilde{x}_1 = \widetilde{x}_{i1} + \frac{L}{2}\sin\left(\frac{2\widetilde{t}}{L}\right) \quad \text{and} \quad \widetilde{x}_2 = \widetilde{x}_{i2} + \frac{L}{2}\sin\left(\frac{2\widetilde{t}}{L} + \alpha\right)$$

NUMERICAL METHODS AND SOLUTION PROCEDURES

The solution methods for solving these above equations use the framework concept of the two-stage pressure-correction method proposed by Cheng and Hung [14]. The methods are described briefly in the following.

Two-stage pressure corrections

First-stage pressure correction. To calculate all the variables simultaneously, a staggered grid system suggested by Patankar [20] is employed. For each variable, the algebraic discretization equations are constructed by discretizing the integral governing equations over the grid cells.

The SIMPLEC method, proposed by Van Doormaal and Raithby [21], and the power-law scheme [20] has been modified here to form the first stage of pressure correction. The purpose of the first-stage pressure correction is to improve the guessed pressure $\widetilde{P}^{**}$ such that the updated velocity and density fields will progressively approach the solutions satisfying the continuity equation. Thus, using the concept suggested in References [20, 21], let

$$\widetilde{P}^{*} = \widetilde{P}^{**} + \widetilde{P}' \tag{11}$$

where $\widetilde{P}^{*}$ and $\widetilde{P}^{**}$ indicate the updated and the guessed pressures, respectively, and $\widetilde{P}'$ is the pressure correction. The density and velocity components respond to the correction of pressure with

$$\widetilde{\rho}^{*} = \widetilde{\rho}^{**} + \widetilde{\rho}' \tag{12a}$$

$$\widetilde{u}^{*} = \widetilde{u}^{**} + \widetilde{u}' \tag{12b}$$

$$\widetilde{v}^{*} = \widetilde{v}^{**} + \widetilde{v}' \tag{12c}$$

According to Equation (7), the relation between $\widetilde{\rho}'$ and $\widetilde{P}'$ can be described approximately by

$$\widetilde{\rho}' \sim \frac{C\widetilde{P}'}{\widetilde{T}} \tag{13}$$

The correction terms of velocity components $\widetilde{u}'$ and $\widetilde{v}'$ can be related to the pressure correction by letting

$$\widetilde{\rho}^{**}\widetilde{u}' \sim -\Lambda \frac{\partial \widetilde{P}'}{\partial \widetilde{x}} \tag{14a}$$

$$\widetilde{\rho}^{**}\widetilde{v}' \sim -\Lambda \frac{\partial \widetilde{P}'}{\partial \widetilde{y}} \tag{14b}$$

The value of Λ should be determined at all the faces of the grid cells. Introducing Equation (11) into the discretized continuity equation and following a procedure similar to those described in References [20, 21], one obtains the first-stage pressure-correction equation ($\widetilde{P}'$-equation) as well as the relations for Λ.

Using the first-stage pressure-correction equation, a solution for $\widetilde{P}'$ can be obtained. However, the updated pressure $\widetilde{P}^{*}$ obtained in the first-stage pressure correction is not necessarily the absolute pressure since $\widetilde{P}'$ and $\widetilde{P}' + C$ (C is an arbitrary constant) would both satisfy the $\widetilde{P}'$-equation. However, unless the solution of the absolute pressure is carried out, density and temperature of the gas must not be accurately evaluated. Further correction for the updated pressure $\widetilde{P}^{*}$ is required to yield the absolute pressure. Therefore, the second-stage pressure-correction method described by Cheng and Hung [14] is used to yield the absolute dimensionless pressure field.

Second-stage pressure correction. The updated pressure is improved by adding a constant value $\widetilde{P}_0$ as

$$\widetilde{P}^{*n+1} = \widetilde{P}^{*n} + \widetilde{P}_0 \tag{15}$$

where $\widetilde{P}^{*_{n+1}}$ is the updated dimensionless absolute pressure and the superscript n denotes the nth step of iteration. Note that the velocity field satisfying the mass and momentum equations is not altered at this stage by the addition of $\widetilde{P}_0$.

During the reciprocating compression and expansion process, the state of the matter within the cylinder changes continuously, but the total amount of mass enclosed in the system remains constant. That is, in dimensionless form

$$\iint \widetilde{\rho}(\widetilde{P}, \widetilde{T})\, \mathrm{d}\widetilde{x}\, \mathrm{d}\widetilde{y} = \text{constant} = \widetilde{m} \tag{16}$$

The amount of mass $\widetilde{m}$ is calculated based on the density distribution at the initial state defined by the hydrostatic condition:

$$\widetilde{m} = \frac{1}{\rho_{\mathrm{R}} H^2} \iint \rho_{\mathrm{E}}\, \mathrm{d}x\, \mathrm{d}y \tag{17}$$

Meanwhile, the tentative mass at each time step is calculated by

$$\widetilde{m}^* = \iint \widetilde{\rho}(\widetilde{P}^{*_{n+1}}, \widetilde{T})\, \mathrm{d}x\, \mathrm{d}y \tag{18}$$

The density field is updated by introducing the updated absolute pressure until the requirement of the mass conservation is fulfilled. That is,

$$\left| \frac{\widetilde{m}^* - \widetilde{m}}{\widetilde{m}} \right| = \left| \frac{\iint \widetilde{\rho}(\widetilde{P}^{*_n} + \widetilde{P}_0, \widetilde{T})\, \mathrm{d}\widetilde{x}\, \mathrm{d}\widetilde{y} - \widetilde{m}}{\widetilde{m}} \right| \leqslant \varepsilon \tag{19}$$

The value of $\widetilde{P}_0$ is determined by means of a shooting method until the requirement that the overall mass of air should be equal to the initial mass is satisfied. The tentative mass at each time step is calculated and the density field is updated by introducing the updated absolute pressure until the requirement of the overall mass conservation is fulfilled. In this study, the mass residue for the overall mass conservation is set to be 10^{-10}. By doing so, the results are expected to provide not only the velocity field agreeing with the continuity and the momentum equations, but also the correct absolute pressure information leading to the exact overall mass.

In the present study, the computation has been performed by using 53×53 grids in the solution domain. The enclosure volume experiences compression and expansion periodically due to the relative motion of the walls with phase angle α. At any instant, the grid lines divide the new domain into a fixed number of control cells whose positions and volumes vary with time. The moving grids deform in resonance with the walls to accommodate the variation in the volume of the enclosure. Typically, the magnitude of $\Delta\widetilde{t}$ would have to be sufficiently small so that the Courant number ($\Delta\widetilde{t}\widetilde{u}_{\mathrm{b}}/\Delta\widetilde{x}$) will be much less than unity. Therefore, $\Delta\widetilde{t}$ is chosen to ensure the satisfaction with this condition.

Effects of the frequency, stroke, and the phase angle of the wall oscillations on the flow are of major concerns. In this study, the frequency is ranged between 5 and 25 Hz and the dimensionless strokes (l/H) of the wall are varied from 0.4 to 1.0. The difference of the dimensionless temperatures, $\widetilde{T}_1 - \widetilde{T}_2$, is fixed at 1.32, corresponding to the practical operation temperatures of approximately $T_{\mathrm{H}} = 700\,\mathrm{K}$ and $T_{\mathrm{R}} = 300\,\mathrm{K}$. These parameters are assigned

Table I. Analysed cases.

Case	Phase angle α	Frequency f [Hz]	Stroke l/H	$\widetilde{T}_1 - \widetilde{T}_2$
1	0	15	0.8	1.32
2	$\pi/6$	15	0.8	1.32
3	$\pi/3$	15	0.8	1.32
4	$\pi/2$	15	0.8	1.32
5	$2\pi/3$	15	0.8	1.32
6	$5\pi/6$	15	0.8	1.32
7	π	15	0.8	1.32
8	$7\pi/6$	15	0.8	1.32
9	$4\pi/3$	15	0.8	1.32
10	$3\pi/2$	15	0.8	1.32
11	$5\pi/3$	15	0.8	1.32
12	$11\pi/6$	15	0.8	1.32
13	$\pi/2$	5	0.4	1.32
14	$\pi/2$	5	0.6	1.32
15	$\pi/2$	5	0.8	1.32
16	$\pi/2$	5	1.0	1.32
17	$\pi/2$	10	0.4	1.32
18	$\pi/2$	10	0.6	1.32
19	$\pi/2$	10	0.8	1.32
20	$\pi/2$	10	1.0	1.32
21	$\pi/2$	15	0.4	1.32
22	$\pi/2$	15	0.6	1.32
23	$\pi/2$	15	1.0	1.32
24	$\pi/2$	25	0.4	1.32
25	$\pi/2$	25	0.6	1.32
26	$\pi/2$	25	0.8	1.32
27	$\pi/2$	25	1.0	1.32

in accordance with the specifications and operation conditions of a laboratory-scale Striling engine developed by Cheng and coworkers [22]. The combined influence of the movement of the walls and the buoyancy as well on the convective heat transfer and the input power required to move the walls is evaluated. The cases analysed herein are listed in Table I.

RESULTS AND DISCUSSION

Magnitude of Nusselt number represents the heat transfer performance between the hotter and the colder walls, and the obtained numerical solutions for the temperature distributions enable the heat transfer performance to be further estimated. Nusselt numbers on the moving, vertical, isothermal walls are given by

$$Nu_1(\widetilde{t}) = \frac{h_1(t)H}{k} \tag{20a}$$

and

$$Nu_2(\widetilde{t}) = \frac{h_2(t)H}{k} \tag{20b}$$

respectively, where the heat transfer coefficients on the isothermal walls, h_1 and h_2, are defined by

$$h_i(t) = -\frac{k}{H(T_H - T_R)} \int_0^H \left.\frac{\partial T(t)}{\partial x}\right|_i \mathrm{d}y, \quad i = 1, 2 \tag{21}$$

Average Nusselt numbers are determined, when the periodically stable periods are reached, by the following equation:

$$\overline{Nu_i} = \frac{\bar{h}_i H}{k} = \frac{1}{\tilde{t}_P} \int_{\tilde{t}}^{\tilde{t}+\tilde{t}_P} Nu_i \, \mathrm{d}\tau \tag{22}$$

where $\tilde{t}_P$ is a dimensionless period of wall oscillation. Based on energy conservation principle, the input power to the system required to excite the oscillation of the walls is equal to the net output heat transfer rate to the surroundings. That is,

$$\dot{W} = \dot{Q}_2 - \dot{Q}_1 \tag{23}$$

where $\dot{Q}_i = \bar{h}_i H(T_H - T_R)$. Introduction of Equation (22) into Equation (23) yields

$$\dot{\tilde{W}} = \overline{Nu_2} - \overline{Nu_1} \tag{24}$$

where $\dot{\tilde{W}}$ is the dimensionless input power defined by

$$\dot{\tilde{W}} = \frac{(Q_2 - Q_1)H}{k(T_H - T_R)}$$

Integration of input power with respect to time in a period of oscillation leads to the results of input work per cycle. Therefore, one can readily calculate the required dimensionless input work per cycle by

$$\tilde{W} = \int_{\tilde{t}}^{\tilde{t}+\tilde{t}_P} \dot{\tilde{W}} \, \mathrm{d}\tilde{t} \tag{25}$$

Figure 2 shows the transient variations of the dimensionless quantities, $\tilde{P}$, $\tilde{T}$, $\tilde{u}$ and $\tilde{v}$ in the periodically stable periods, for case 4 with $f = 15$ Hz, $l/H = 0.8$ and $\alpha = \pi/2$. All values are taken at the centre point of the enclosure. Note that the location of the centre point is actually moved with time due to transient change of the enclosure space. It is observed that all the quantities exhibit a periodic feature at the same frequency of the oscillation of the walls. As shown in Figure 2(b), the dimensionless temperature at the centre point of enclosure oscillates approximately between 1.65 and 2.05 with an average of 1.82, which is higher than the average value of the isothermal wall temperatures (1.66). This is attributed to the power input in the compression and expansion processes that increases the internal energy of the air in the enclosure. It is found that the dimensionless temperature oscillates with the dimensionless pressure without a time lag. In addition, the magnitude of $\tilde{u}$ is much greater than that of $\tilde{v}$ since the walls oscillate in the x-direction.

In order to have a deeper insight of the cyclic variation in the flow and thermal fields, a number of snapshots of the velocity and the temperature distributions in a cycle in the periodically stable region for cases 4 and 15 with $l/H = 0.8$ and $\alpha = \pi/2$ are shown in

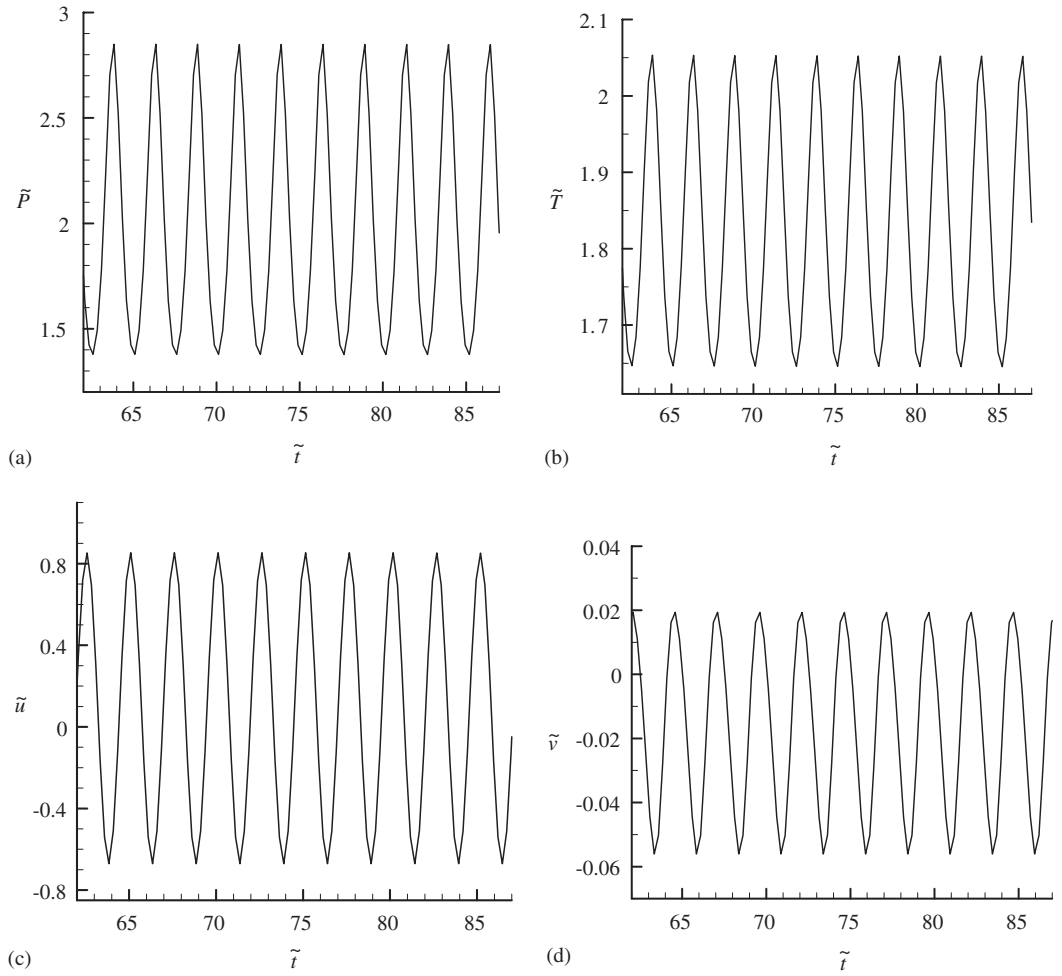

Figure 2. Periodic variation of dimensionless quantities for case 4, with $f = 15\,\text{Hz}$, $l/H = 0.8$ and $\alpha = \pi/2$, in the periodically stable periods. All values are taken at the centre point of the enclosure at any instant.

Figures 3 and 4, respectively. The moving frequency of case 4 is 15 Hz. The flow field is illustrated by plotting the velocity vectors, and the thermal field by plotting the isotherms. During the period in the cyclic process from $\tilde{t} = \tilde{t}_0$ to $\tilde{t} = \tilde{t}_0 + 0.4\tilde{t}_P$, in Figure 3 the dimensionless temperature reaches a maximum of 2.50 during the compression process. Being reminded of that the dimensionless temperature on the hotter wall is 2.32, one readily expects a possibility of heat transfer output to the surroundings through the hotter walls. In the expansion process after $\tilde{t} = \tilde{t}_0 + 0.5\tilde{t}_P$, the dimensionless temperature in the whole volume is decreased. It is noticed that although the walls are under the influence of wall movement, the buoyancy effects leading to the thermal boundary layers along the vertical walls are still observed.

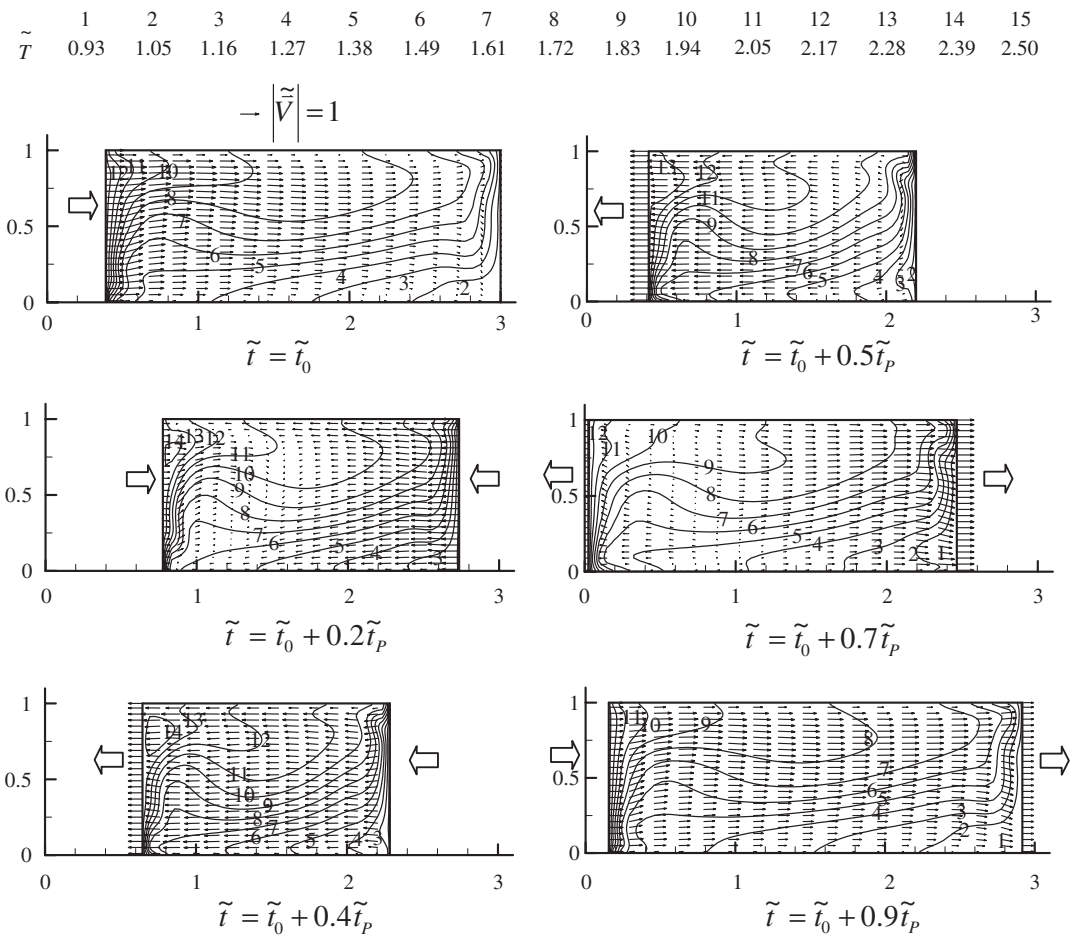

Figure 3. Snapshots of velocity and temperature distributions in a cycle in the stable region for case 4, at $\alpha = \pi/2$, $f = 15\,\text{Hz}$, $l/H = 0.8$, and $\tilde{T}_1 - \tilde{T}_2 = 1.32$.

Figure 4 shows the variations in the flow and the thermal fields at a lower frequency $f = 5\,\text{Hz}$ with case 15. At this frequency, it is found that the dimensionless temperature reaches a maximum of only 2.41 in the compression process. However, the flow in the enclosure is still greatly affected by the driving effects of the moving walls; therefore, the velocity vectors of the fluid adjacent to the two moving walls are nearly in resonance with the moving velocity.

Figure 5 shows the variations in the Nusselt numbers on the moving walls for cases 15, 4, and 26, with $f = 5$, 15 and 25 Hz, respectively, at $l/H = 0.8$ and $\alpha = \pi/2$. Nusselt number results on both the hotter and the colder walls are plotted. It is observed that the periodic motion of the walls results in oscillation of the Nusselt numbers. As the oscillation frequency is increased from 5 to 15 Hz, the amplitudes of the oscillation of the Nusselt numbers are

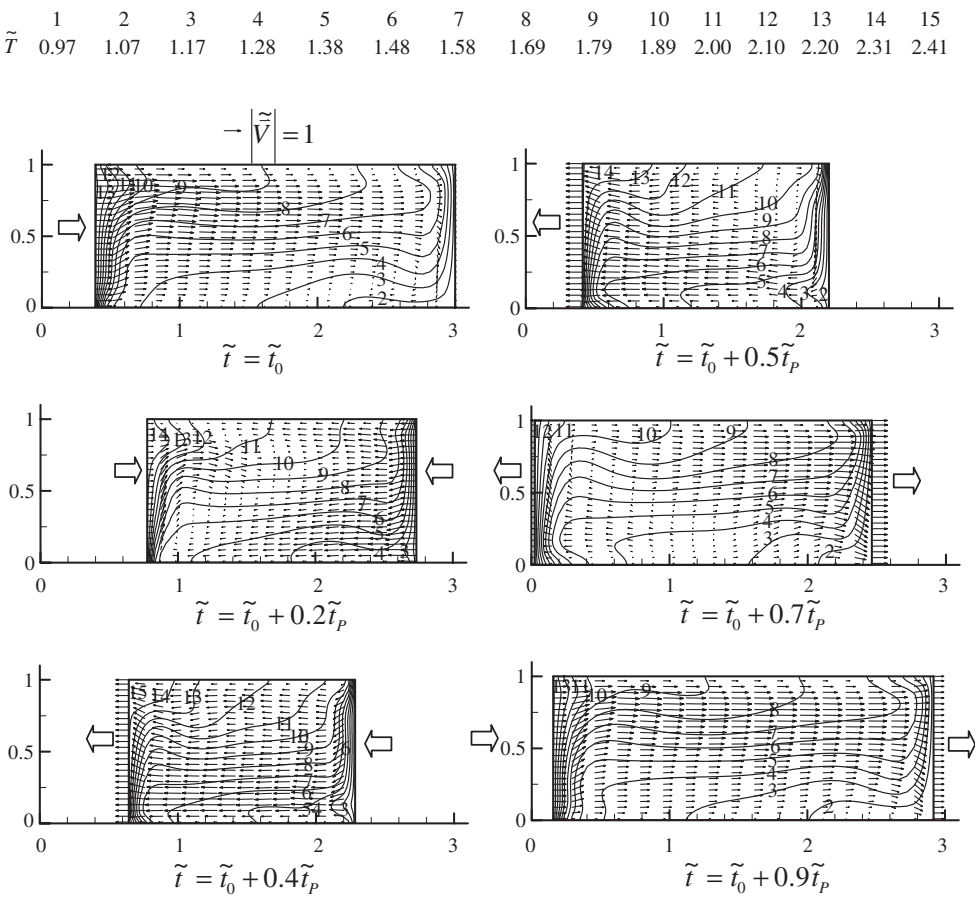

Figure 4. Snapshots of velocity and temperature distributions in a cycle in the stable region for case 15, at $\alpha = \pi/2$, $f = 5\,\text{Hz}$, $l/H = 0.8$, and $\tilde{T}_1 - \tilde{T}_2 = 1.32$.

remarkably elevated. When the frequency is further increased to be 25 Hz, the amplitudes of the oscillation of the Nusselt numbers continue to increase. It is noticed that the Nusselt number on the hotter wall (Nu_1) appears to be negative in some certain periods of time, as seen in Figure 5(c). A negative Nusselt number on the hotter wall indicates that heat could also be rejected to the surroundings through the hotter wall once the fluid temperature becomes higher than T_H, as already mentioned earlier. In the high-frequency cases, more power input is consumed to maintain the wall oscillation, and the compression and expansion processes are severer; therefore, in these cases the fluid temperature exceeds the hotter wall temperature T_H.

Figure 6 shows the variations in dimensionless input power ($\dot{\tilde{W}}$) as a function of the phase angle (α) at $f = 15$, $l/H = 0.8$, and $\tilde{T}_1 - \tilde{T}_2 = 1.32$, by showing the results associated with cases 1–12. The values of $\dot{\tilde{W}}$ are calculated by Equation (15) and indicated with circles in this

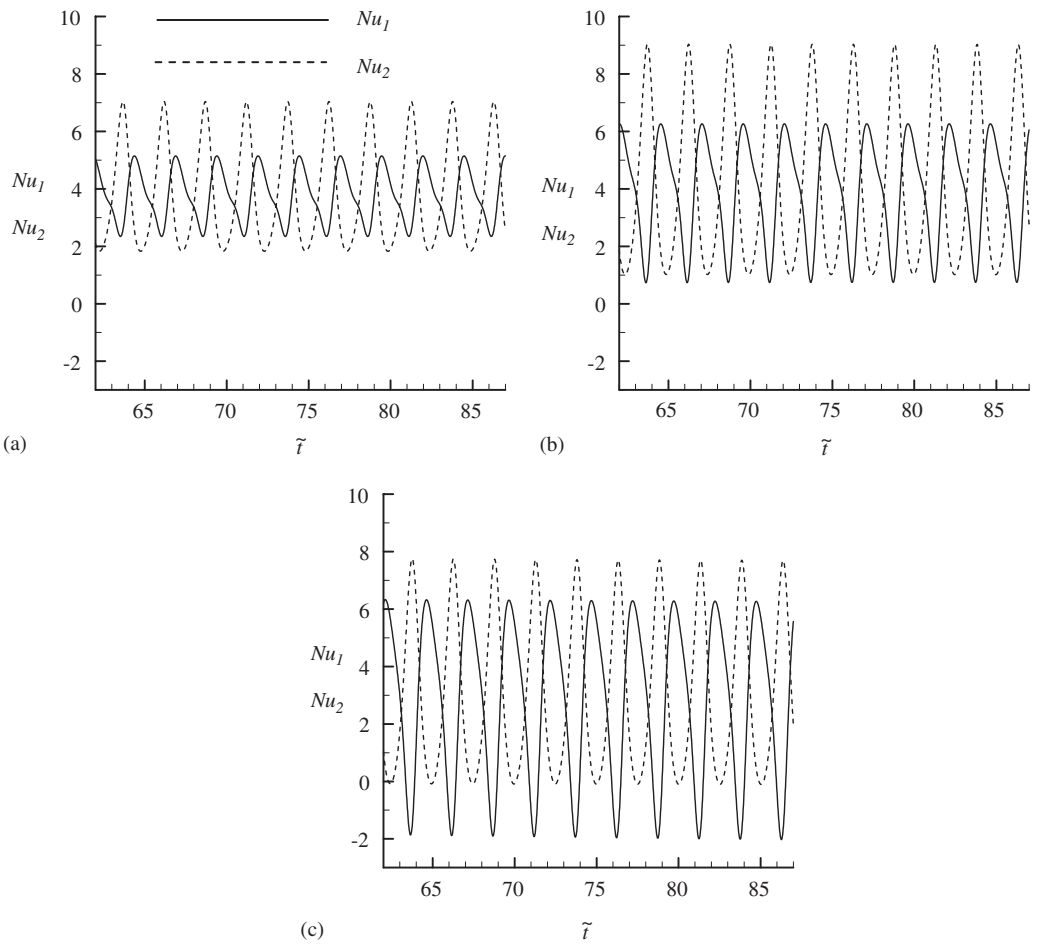

Figure 5. Transient variations in Nusselt numbers at different frequencies in the periodically stable periods, at $\alpha = \pi/2$ Hz, $l/H = 0.8$, and $\widetilde{T}_1 - \widetilde{T}_2 = 1.32$ (a) $f = 5$ Hz (case 15); (b) $f = 15$Hz (case 4); and (c) $f = 25$Hz (case 26).

figure. For the zero-phase-angle cases, both vertical walls move at the same speed and in the same direction, and therefore the volume of the enclosure is moving but not deforming. In this situation, the volume of the enclosure keeps constant so that the dimensionless power input required for compression and expansion in a cycle is zero. As the phase angle is increased to π, the dimensionless power input reaches a peak value of 0.54. This is because in the case of $\alpha = \pi$, the two vertical walls move in opposite directions exactly and hence, the magnitude of the compression ratio, defined by the ratio of the maximum volume to the minimum in a cycle, is higher than other cases. When the value of the phase angle is further elevated from π to 2π, the dimensionless power input is gradually decreased to zero since the case at $\alpha = 2\pi$ is identical to the one at $\alpha = 0$.

Figure 7 shows the results of the dimensionless input work per cycle ($\widetilde{W}$) as a function of dimensionless stroke and frequency. Cases 4, and 13–27, all fixed at $\alpha = \pi/2$ and $\widetilde{T}_1 - \widetilde{T}_2 = 1.32$,

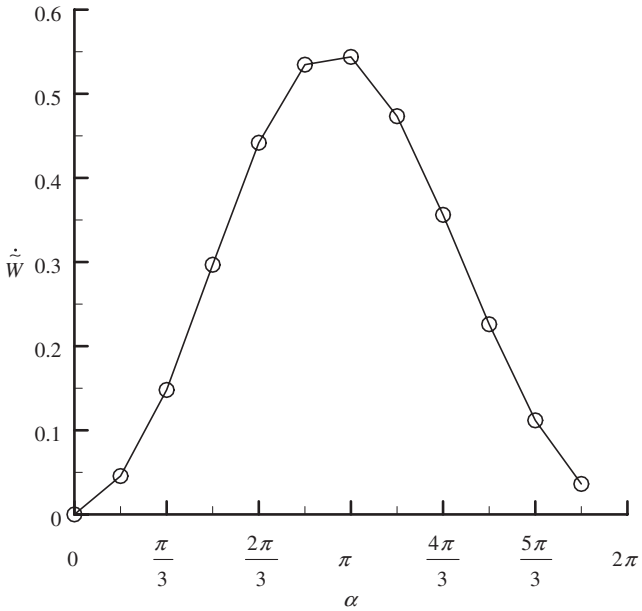

Figure 6. Dimensionless input power as a function of phase angle α. Cases 1–12 are considered herein, at $f = 15\,\text{Hz}$, $l/H = 0.8$, and $\tilde{T}_1 - \tilde{T}_2 = 1.32$.

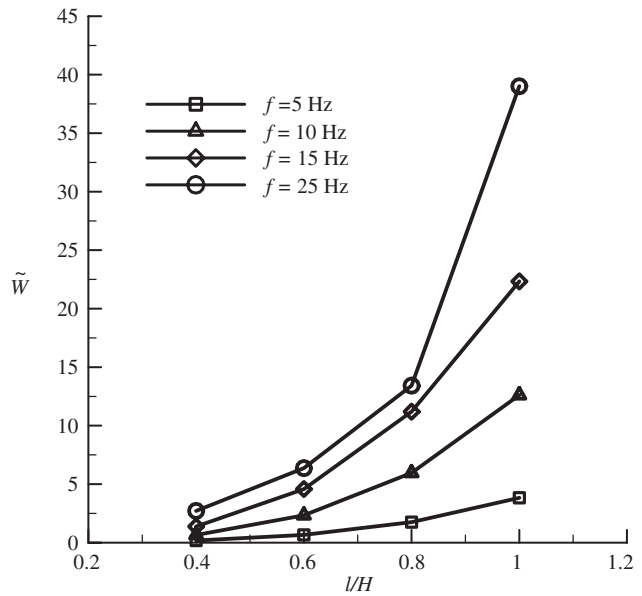

Figure 7. Dimensionless input work per cycle as a function of dimensionless stroke and frequency. Cases 4, and 13–27 are considered herein, at $\alpha = \pi/2$ and $\tilde{T}_1 - \tilde{T}_2 = 1.32$.

are considered in this figure. It is found that the value of the dimensionless input work per cycle increases with the dimensionless stroke. Furthermore, for the cases with l/H varied from 0.4 to 1.0, an increase in frequency also results in an increase in $\widetilde{W}$. A comparison between cases 16 and 27 in Table I shows that when the frequency is elevated from 5 to 25 Hz at high vibrating stroke $l/H = 1.0$, and the required dimensionless input work per cycle may be remarkably increased from 3.8 to 39.0. In other words, a higher vibration frequency or a higher stroke requires a higher work input per cycle. However, as the dimensionless stroke is within 0.4 and 0.8, an increase in the frequency from 15 to 25 Hz leads to only a slight increase in $\widetilde{W}$.

CONCLUDING REMARKS

The influence of the periodic movement of two vertical isothermal walls on the flow pattern and thermal characteristics of the mixed convective flows in a rectangular enclosure is predicted numerically. Effects of the frequency, stroke, and the phase angle of the wall oscillations on the flow are evaluated. In this study, the frequency is ranged between 5 and 25 Hz and the dimensionless strokes (l/H) of the wall are varied from 0.4 to 1.0. Results regarding the Nusselt numbers on the walls and the dimensionless input work required to excite the wall oscillation are provided.

It is observed that all the quantities of $\widetilde{P}$, $\widetilde{T}$, $\widetilde{u}$ and $\widetilde{v}$ exhibit a periodic feature at the same frequency of the oscillation of the walls in the periodically stable periods. The dimensionless temperature oscillates with the dimensionless pressure without a time lag. In addition, the magnitude of $\widetilde{u}$ is much greater than that of $\widetilde{v}$ since the walls oscillate in the x-direction. The periodic motion of the walls also results in oscillation of the Nusselt numbers. As the oscillation frequency is increased, the amplitudes of the oscillation of the Nusselt numbers are remarkably elevated. In addition, at a higher frequency, the Nusselt number on the hotter wall (Nu_1) may appear to be negative in some certain periods of time since heat could also be rejected to the surroundings through the hotter wall once the fluid temperature becomes higher than T_H in the compression processes.

As the phase angle is assigned to be $\alpha = \pi$, the dimensionless power input reaches a peak value. This is because in that case, the two vertical walls move in opposite directions exactly and hence, the magnitude of the compression ratio is higher than other cases. On the other hand, in the cases of $\alpha = 0$ and 2π, the volume of the enclosure keeps constant, and therefore the dimensionless power input required for compression and expansion in a cycle is zero. In general, an increase in the frequency or the stroke of the wall oscillation results in an increase in the required work input. However, for some particular cases, an increase in the frequency leads to only a slight increase in the cyclic work input.

NOMENCLATURE

C_P constant-pressure specific heat of air
D the distance between two moving walls
f frequency of the wall motion [Hz]
g gravitational acceleration
h heat transfer coefficient

H height of the vertical wall
l stroke of moving walls
L dimensionless stroke of moving walls, l/H
Nu Nusselt number, hH/k
$\overline{Nu}$ average Nusselt number
P absolute pressure
$\widetilde{P}$ dimensionless pressure, $(P - P_{\mathrm{E}})/(\rho_{\mathrm{R}} U_{\mathrm{R}}^2)$
$\widetilde{P}_{\mathrm{E}}$ dimensionless hydrostatic pressure, $P_{\mathrm{E}}/(\rho_{\mathrm{R}} R T_{\mathrm{R}})$
$\widetilde{P}_0$ second-stage dimensionless pressure correction
$\widetilde{P}'$ first-stage dimensionless pressure correction
Q heat transfer rate
R gas constant of air
Re Reynolds number, $U_{\mathrm{R}} H/v$
t time
$\widetilde{t}$ dimensionless time, tU_{R}/H
$\widetilde{t}_P$ dimensionless period of wall oscillation
T temperature
T_{H} hotter wall temperature
T_{R} colder wall temperature
$\widetilde{T}$ dimensionless temperature, T/T_{R}
u, v velocity components in x- and y-directions
$\widetilde{u}, \widetilde{v}$ dimensionless velocity components, u/U_{R} and v/U_{R}
U_{R} characteristic velocity, $\pi f l$
$\widetilde{\mathbf{V}}, \widetilde{V}$ dimensionless velocity vector
$\dot{W}$ input power
$\widetilde{\dot{W}}$ dimensionless input power
$\widetilde{W}$ dimensionless input work per cycle
x, y Cartesian coordinates
$\widetilde{x}, \widetilde{y}$ dimensionless Cartesian coordinates, x/H and y/H

Greek symbols

α phase angle of moving walls
v kinematic viscosity of air
ρ density of air
ρ_{R} reference density
$\widetilde{\rho}$ dimensionless density of air, ρ/ρ_{R}

Subscripts

1 left wall
2 right wall
B bottom-dead point
b face of grid cell
E hydrostatic condition
T top-dead point

REFERENCES

1. Hirt CW, Amsden AA, Cook JL. An arbitrary Lagrangian–Eulerian computing method for all flow speeds. *Journal of Computational Physics* 1974; **14**:227–253.
2. Demirdzic I, Peric M. Finite volume method for prediction of fluid flow in arbitrarily shaped domains with moving boundary. *International Journal for Numerical Methods in Fluids* 1990; **10**:771–790.
3. Gosman AD. Prediction of in-cylinder process in reciprocating internal combustion engines. In *Computer Methods in Applied Science and Engineer*, Glowinski R, Lions JL (eds). Elsevier: Amsterdam, 1984; 609–629.
4. Hirt CW, Nichols BD. Volume of fluid (VOF) method for the dynamics of free boundaries. *Journal of Computational Physics* 1981; **39**:201–225.
5. Haworth DC, Jansen K. Large-eddy simulation on unstructured deforming meshes: towards reciprocating IC engines. *Computers and Fluids* 2000; **29**:493–524.
6. Nkonga B. On the conservative and accurate CFD approximations for moving meshes and moving boundaries. *Computer Methods in Applied Mechanics and Engineering* 2000; **190**:1801–1825.
7. Trulio JG, Trigger KR. Numerical solution of the one-dimensional hydrodynamic equation in an arbitrary time-dependent coordinate system. *Lawrence Radiation Laboratory Report UCLR-6522*, University of California, 1961.
8. Demirdzic I, Peric M. Space conservation law in finite volume calculations of fluid flow. *International Journal for Numerical methods in Fluids* 1988; **8**:1037–1050.
9. Zwart PJ, Raithby GD, Raw MJ. An integrated space-time finite-volume method for moving-boundary problems. *Numerical Heat Transfer*, *Part B* 1998; **34**:257–270.
10. Guillard H, Farhat C. On the significance of the geometric conservation law for flow computations on moving meshes. *Computer Methods in Applied Mechanics and Engineering* 2000; **190**:1467–1482.
11. Falcovitz J, Alfandary G, Hanoch G. A two-dimensional conservation laws scheme for compressible flows with moving boundaries. *Journal of Computational Physics* 1997; **138**:83–102.
12. Koobus B, Farhat C. Second-order time-accurate and geometrically conservative implicit schemes for flow computations on unstructured dynamic meshes. *Computer Methods in Applied Mechanics and Engineering* 1999; **170**:103–129.
13. Visbal MR, Gaitonde DV. On the use of higher-order finite-difference schemes on curvilinear and deforming meshes. *Journal of Computational Physics* 2002; **181**:155–185.
14. Hung KS, Cheng CH. Numerical predictions of flow and thermal fields in a reciprocating piston-cylinder assembly. *Numerical Heat Transfer*, *Part A* 2000; **38**:397–421.
15. Hung KS, Cheng CH. Pressure effects on natural convection for non-boussinesq fluid in a rectangular enclosure. *Numerical Heat Transfer*, *Part A* 2002; **41**:515–528.
16. Liu CH, Cheng CH, Hung KS, Lin PL. Thermal-fluid analysis of stirling engines. *Proceedings of the 20th National Conference of the CSME*, Taipei, Taiwan, R.O.C., 5–6 December 2003.
17. Shih CC, Cheng CH, Lin PL. Mechanism design and thermal-fluid analysis of stirling engines using rhombic drive. *Proceedings of the 21st National Conference of the CSME*, Kaoshong, Taiwan, R.O.C., November 26–27 2004.
18. Cheng CH. Strengthening connection between theories and engineering practice via miniature stirling engines. In *Innovations 2005—World Innovations in Engineering Education and Research* (Chapter 12), Aung W *et al*. (eds). iNEER, Begell House Publishing: New York, 2005.
19. Stine WB, Diver RE. A compendium of solar dish stirling technology. *Report SAND94-7026*, Sandia National Laboratories, Albuquerque, NM 87185, 1994.
20. Patankar SV. *Numerical Heat Transfer and Fluid Flow.* Hemisphere: Washington, DC, 1980.
21. Van Doormaal JP, Raithby CD. Enhancements of the SIMPLE method for predicting incompressible fluid flow. *Numerical Heat Transfer* 1984; **7**:147–163.
22. Cheng CH, Lin YH, Lin TA, Lin C, Hsiao YC. Study of rhombic-drive coaxial piston-displacer stirling engine. *Proceedings of the 29th National Conference on Theoretical and Applied Mechanics*, Hsinchu, Taiwan, R.O.C., 16–17 December 2005.

